energies

MDPI

Article

Enhancing the Power Performance of Latent Heat Thermal Energy Storage Systems: The Adoption of Passive, Fractal Supports

Giorgio Amati [1], Sauro Succi [2,3] and Giacomo Falcucci [3,4,*]

[1] High Performance Computing Department, CINECA Rome Section, 00185 Rome, Italy; g.amati@cineca.it
[2] Italian Institute of Technology, Center for Life Nano- and Neuro-Science, 00161 Rome, Italy; sauro.succi@iit.it
[3] Department of Physics, Harvard University, Cambridge, MA 02138, USA
[4] Department of Enterprise Engineering "Mario Lucertini", University of Rome "Tor Vergata", 00133 Rome, Italy
* Correspondence: giacomo.falcucci@uniroma2.it

Abstract: We employ a three-phase thermal lattice Boltzmann model (LBM) to investigate the power performance of latent heat thermal energy storage (LHTES) systems based on the exploitation of phase change materials (PCMs). Different passive thermal supports are considered to increase the melting rate, including innovative, fractal, branch-like structures. Our simulations reveal that the adoption of fractal, branch-like metal supports consistently outperforms other configurations in terms of PCM melting rates. These results open the path towards novel strategies to enhance the power performance of PCM-based TES systems, offering potential benefits for energy storage applications.

Keywords: PCM; TES; hydrogen storage; metal hydrides; lattice Boltzmann method

Citation: Amati, G.; Succi, S.; Falcucci, G. Enhancing the Power Performance of Latent Heat Thermal Energy Storage Systems: The Adoption of Passive, Fractal Supports. *Energies* **2023**, *16*, 6764. https://doi.org/10.3390/en16196764

Academic Editor: Armando Oliveira

Received: 31 July 2023
Revised: 5 September 2023
Accepted: 19 September 2023
Published: 22 September 2023

1. Introduction

Thermal energy storage (TES) systems are the object of extensive research efforts, in recent years, as promising contributors to increasing the sustainability of heating and cooling [1]. In the EU, in fact, domestic heating and hot water production account for almost 80% of total energy use [1], while worldwide heat contributes to 40% of total CO_2 emissions [2].

TES systems based on phase change materials (PCMs), also known as latent heat TES (LHTES), can store large amounts of waste heat at almost constant temperature, providing an ideal solution for technical applications that require thermal baths [3–5], including hydrogen storage via metal hydrides [6,7]. The drawbacks of LHTES systems are typically related to (i) incongruent melting/phase separation, (ii) subcooling, and (iii) low thermal conductivity, delivering limited heat transfer rates and poor power performance [8,9]. To increase the thermal conductivity of the PCM matrix, several strategies are explored in the literature that can essentially be grouped in the following categories [9]:

- Realization of optimized blends of PCMs: blends can be formulated in the attempt to get the desired PCM thermal properties to better suit the designed application [10];
- Adoption of highly conductive thermal supports: realized in the forms of fins, blades, heat pipes, and foams [11]. Their exploitation strongly enhances thermal conductivity (>200×, when embedding the PCM in porous graphite [12,13]), but can lead to detachment phenomena between the PCM and the thermal support. This phenomenon is due to the volumetric variation during melting/solidification and causes poor performance in repeated cycles [14];
- Addition of micro-/nano-particles: the adoption of micro/nano-particles, nano-fibers, nano-tubes, and other nano-scale fillers can actually provide remarkable enhancements in specific heat, thermal conductivity, and thermal diffusivity (pristine graphene allows an increase in thermal conductivity up to 2800% [15,16]);

- Encapsulation: an expensive procedure that can even turn into the opposite result, increasing the overall thermal resistance, through the insertion of the coating layer [9]; moreover, the stability of the coating for repeated melting/solidification in time is still an open issue [17].

This study aims at investigating the enhancement of power performance of TES systems by utilizing solid thermal supports to increase the melting rate of phase change materials. More specifically, we study the melting rate performance of PCMs at low to intermediate Rayleigh numbers, $0 < \mathrm{Ra} < 10^6$, through an ad hoc designed numerical platform based on the lattice Boltzmann method (LBM) [18,19]. The proposed approach capitalizes on the model developed in [20] and extended in [7]. LBM has proven flexible and reliable in simulating different complex systems at the intersection between engineering, physics, and biology [21–27], thus providing an efficient and computationally light alternative to Navier–Stokes-based computational frameworks. Recently, LBM has been also applied to conjugate heat transfer problems, delivering interesting and reliable predictions [20,28–31].

To evaluate the impact of the morphology of the thermal support, we conduct our simulations considering different layouts of thermal solid supports. The adoption of such supports is known from the literature as one of the strategies to improve the typical drawback of PCM systems, namely their reduced thermal conductivity [9]. However, no final solutions have been found in the literature to date, with several authors proposing their own layout, in the form of thin blades, thicker fins, porous structures, and even graphitized networks [32]. Fins and blades represent the simplest structures for thermal conductivity enhancement. They do not suffer from filling problems, such as the porous structures, and allow the onset of convective motions [33]. However, the adoption of fins and blades can lead to PCM detachments during repeated melting and solidification processes [14]. Fractal structures represent a novelty in the panorama of thermal supports [34]. Such solutions prove capable of decreasing the PCM thermal lag and increasing the PCM solidification rate during the heat-discharge process, thanks to their high surface-to-volume ratio compared to more conventional designs [34].

Here, we further develop the concept of fractal thermal supports by introducing novel branch-like structures that can benefit from the recent developments of 3D-printing technology. The branched layout allows for high surface-to-volume ratios, provides efficient heat transport high mass transfer capability, due to its bifurcations, and allows for the onset of convective motions [33,35], opening the path towards the design and implementation of future, highly efficient thermal energy storage systems.

2. Materials and Methods

We employ a standard 2-population lattice Boltzmann (LB) implementation [18,19,36,37] to describe the thermal and fluid dynamic evolution of our system:

$$f_i(\boldsymbol{x}+\boldsymbol{c}_i, t+1) - f_i(\boldsymbol{x}, t) = \frac{1}{\tau_F}\left[f_i^{eq}(\boldsymbol{x}, t) - f_i(\boldsymbol{x}, t)\right] + \mathscr{F}_B + \mathscr{F}_{Drag} \quad (1)$$

$$g_i(\boldsymbol{x}+\boldsymbol{c}_i, t+1) - g_i(\boldsymbol{x}, t) = \frac{1}{\tau_T}\left[g_i^{eq}(\boldsymbol{x}, t) - g_i(\boldsymbol{x}, t)\right] + \mathscr{F}_{\mathscr{L}} \quad (2)$$

In the above, τ_F is the fluid relaxation time, related to the fluid kinematic viscosity ν through $\tau_F = \frac{\nu}{c_s^2} + \frac{1}{2}$; τ_T is the thermal relaxation time, given by $\tau_T = \frac{\alpha}{c_s^2} + \frac{1}{2}$, with α the thermal diffusivity. The ratio between the two τs provides the characteristic Prandtl number $\mathrm{Pr} = \nu/\alpha$.

Equation (1) governs the system fluid dynamics, and Equation (2) accounts for the thermal evolution. Through this approach, temperature evolves passively, and its effects are transferred to the fluid through ad hoc modeled interactions. The three forcing terms in Equations (1) and (2), in fact, are: $\mathscr{F}_B$ the buoyancy force; $\mathscr{F}_{Drag}$ the fluid-solid interaction, given by an empirical mesoscopic drag to enforce no-flow inside the solid region [20]; and $\mathscr{F}_{\mathscr{L}}$, which provides the latent heat release/absorption during melting/solidification

phenomena, respectively. To compute such forces, the evolution in time of a phase field parameter ϕ that governs the melting/solidification front must be evaluated. More specifically, we consider the following, discretized rate equation:

$$\phi(\boldsymbol{x}, t) = \phi(\boldsymbol{x}, t-1) + \mathscr{R}\,, \tag{3}$$

in which $\mathscr{R}$ provides a reaction term, described in [20]:

$$\mathscr{R}(\boldsymbol{x}, t) = \mathtt{f}_{+}\, K^{+}(\boldsymbol{x}, t)[1 - \phi(\boldsymbol{x}, t-1)] - \mathtt{f}_{-}\, K^{-}(\boldsymbol{x}, t)[1 + \phi(\boldsymbol{x}, t-1)]\,. \tag{4}$$

In the above, $\mathtt{f}_{+}$ and $\mathtt{f}_{-}$ are frequency factors (basically, the inverse time scale for melting and solidification, respectively), and K^{+} and K^{-} are *switch functions* to control the the onset of melting and solidification, respectively, around the critical temperature T_{cr}.

Here, we directly adopt the modified switches proposed in [20]:

$$K^{+}(\boldsymbol{x}, t) = \frac{1}{2}\left[1 + \tanh\left(\frac{T(\boldsymbol{x}, t) - T_{cr} - T_s}{T_w}\right)\right] \times \frac{1}{8}\sum_i \left\{\frac{1}{2}\varpi_i[1 + \phi(\boldsymbol{x} + \boldsymbol{c}_i), t)]\right\}^2 \tag{5}$$

$$K^{-}(\boldsymbol{x}, t) = \frac{1}{2}\left[1 - \tanh\left(\frac{T(\boldsymbol{x}, t) - T_{cr} + T_s}{T_w}\right)\right] \times \frac{1}{8}\sum_i \left\{\frac{1}{2}\varpi_i[1 - \phi(\boldsymbol{x} + \boldsymbol{c}_i), t)]\right\}^2 . \tag{6}$$

Here, T_w controls the energy range of the transition and T_s provides two different activation energies for melting and solidification. In our basic test cases, $T_s = 0$; ϖ_i is a scaling factor, equal to 1 in the horizontal and vertical directions, and equal to $1/\sqrt{2}$ for the diagonal directions [38].

The evolution in time of ϕ provides the three force contributions in Equations (1) and (2):

$$|\mathscr{F}_B| = \beta\, T(\boldsymbol{x}, t)\, \frac{1 + \phi(\boldsymbol{x}, t)}{2} \tag{7}$$

$$\mathscr{F}_{Drag} = -\tilde{\ell}\, \boldsymbol{u}(\boldsymbol{x}, t)\, [1 - \phi(\boldsymbol{x}, t)] \tag{8}$$

$$\mathscr{F}_{\mathscr{L}} = -\frac{\Delta T}{\mathrm{St}}\, \delta\phi\,. \tag{9}$$

In the above, we have:

- $\tilde{\ell}$ is a relaxation parameter, chosen to be on the order of 0.5 to ensure that the relaxation of $\mathscr{F}_{Drag}$ is *faster* than the other dynamics;
- St is the non-dimensional Stefan number, given by $\mathrm{St} = \mathrm{c}\, \frac{T_{liq} - T_{sol}}{\mathscr{L}}$, with c the specific heat and $\mathscr{L}$ the latent heat;
- ΔT is the characteristic temperature difference: we fix $\Delta T = T_{liquid} - T_{solid}$, as in [7].

Figure 1 sketches the thermal support layouts investigated in the following. We assume such structures to be rigid, with constant and fixed temperature for the entire duration of the simulation: this assumption is justified by the thermal conductivity of the metal support, which is two-to-three orders of magnitude larger than that of the PCM [9]. The three thermal supports are characterized by the same mass, i.e., the number of solid nodes in the domain is kept (approximately) constant: in the case with thin fins, we have $N_s = 2520$ solid nodes; $N_s = 2528$ in the case of thick blades, and, finally, $N_s = 2511$ in the case of the branched fractal structure.

We adopt a 200×200, D2Q9 standard lattice, for both the fluid and thermal populations. The grid independence has been assessed through validation against the 1D Stefan problem [7] and the 2D Rayleigh–Bénard convection problem (see Section 3).

We fix boundary conditions for both the f and g populations [19,39]: for the hydrodynamic population, all boundaries and solid thermal supports are set as wall no slip. From the thermal point of view, the left wall and the thermal supports are characterized by a temperature $T_{wall} = T_{liquid} = 283$ K, whereas the solid PCM is initialized at $T_{solid} = 273$ K,

which coincides with the melting temperature. The upper and lower walls are adiabatic, and the right wall is fixed as a zero-gradient for the temperature.

The geometries in Figure 1 are investigated at different regimes, identified by the values of Rayleigh number, $\mathrm{Ra} = \frac{g\,\beta\,\Delta T\,L^3}{\nu^2} = 0$, 10,000, 50,000, and 500,000. In the Ra definition, we have: g the gravity acceleration (directed vertically from top to bottom in Figure 1), β the volumetric expansion coefficient, ΔT the characteristic temperature difference in Equation (9), ν the kinematic viscosity, L the vertical size of the computational domain, and Pr the Prandtl number. To achieve the desired values of Ra, we vary the modulus of g, keeping constant the other parameters. Considering the other relevant non-dimensional numbers, our simulations are conducted with $\mathrm{Pr} = 50$ and $\mathrm{St} = 1$.

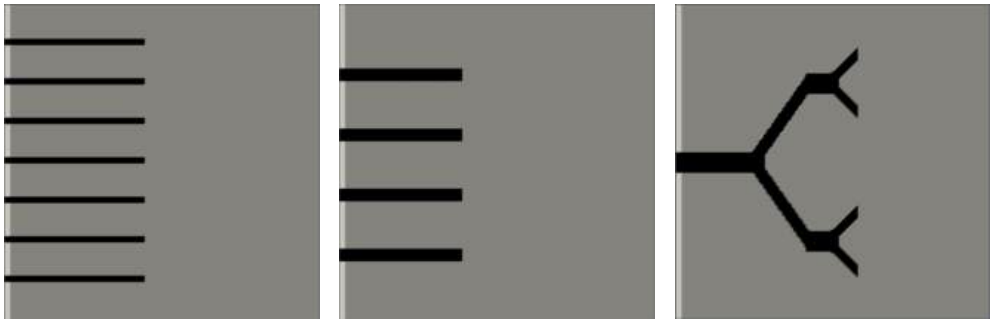

(**a**) (**b**) (**c**)

Figure 1. Sketch of the different morphologies of solid thermal support: (**a**) thin fins; (**b**) thick blades; (**c**) branched fractal structure. The three structures are characterized by the same mass, the same thermal conductivity, and the same temperature.

3. Validation, Results, and Discussion

In the following, we focus on the evolution of the melting front in time. We define the non-dimensional time as $\theta = \mathrm{Fo}\,\mathrm{St}$, with Fo the Fourier number given by $\mathrm{Fo} = \alpha\, t/L^2$ and St the Stefan number in Equation (9).

To validate the model, two classic benchmarks were considered, namely the 1D Stefan problem and the 2D Rayleigh–Bénard convection cell. For the 1D Stefan problem, we have reproduced the results in [28] for three values for thermal diffusivity: $\alpha = 0.033, 0.36$, and 0.70 in lattice units. The cases provide the evolution of the melted front in a quasi-1D case, in which a hot wall melts the solid domain, in absence of gravity acceleration. The top and bottom boundaries are adiabatic, in this case. The Stefan number is the same as in [7,28], $\mathrm{St} = 1$, obtained through $T_{sol} = 273.0$ K, and $T_{liq} = 352.5$ K, in a 100×5 domain. Figure 2a reports the good matching in the 1D case.

Figure 2b shows the steady state plumes of temperature in a Rayleigh–Bénard convection cell. In this case, we consider the presence of gravity acceleration, with periodic boundary conditions on the sides of the domain. The top boundary is cold and the bottom boundary is hot. The simulations reproduce the density plumes due to the counter-action of gravity acceleration and buoyancy [40–42]. The case in Figure 2b refers to $\mathrm{Ra} \sim 3 \times 10^4$ in a 128×64 domain.

Considering the different thermal supports depicted in Figure 1, we report the evolution of the melted faction as a function of the non-dimensional time θ in Figure 3, for different values of the Ra number.

The panels in Figure 3 show that the fractal branches, even with the same mass as the fins and the blades and with the same temperature and thermal conductivity, are always characterized by a faster melting rate in the PCM matrix. This behavior is confirmed also at $\mathrm{Ra} = 500{,}000$, in which the buoyancy effects become predominant and all the thermal supports show a lower performance compared to more moderate Ra values.

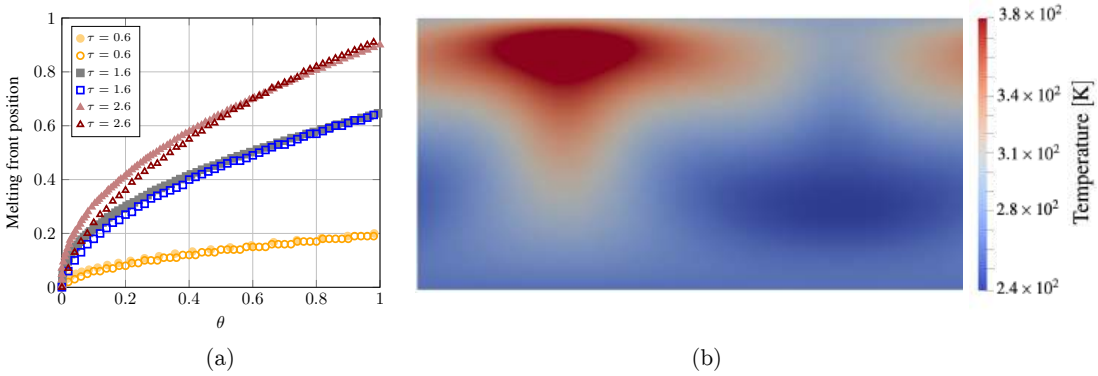

(a) (b)

Figure 2. Validation tests for the LB solver: (**a**) evolution of the melting front in the 1D Stefan problem: in the panel, the filled symbols are taken from [33]; (**b**) steady state plumes of temperature in a 2D Rayleigh–Bénard convection cell [40,42].

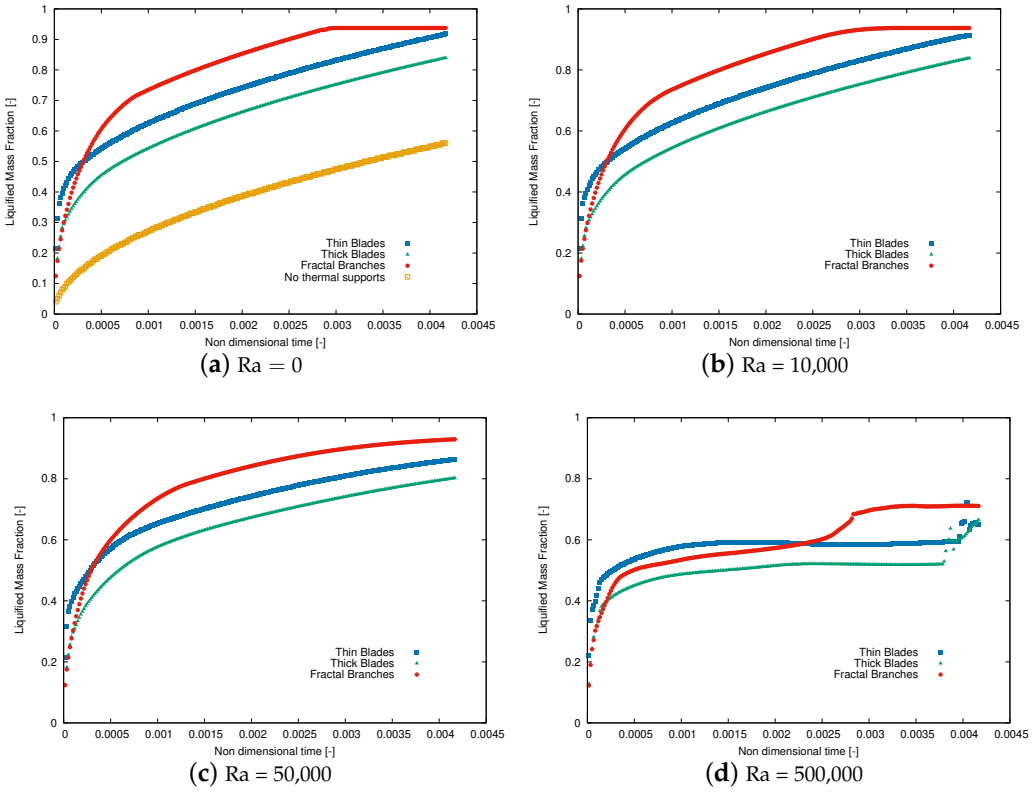

(**a**) Ra = 0 (**b**) Ra = 10,000

(**c**) Ra = 50,000 (**d**) Ra = 500,000

Figure 3. Evolution in time of the liquefied mass fraction inside the computational domain. The effect of the different Ra numbers and of the solid thermal support morphology is apparent.

Figure 4 shows the evolution in time of the phase field ϕ parameter, which represents the liquid and melted phases in the computational domain, at Ra = 0.

From the panel, it is apparent that the presence of thermal supports provides a remarkable increase in the melting rate (as reported in Figure 3a) and that the branched structure increases the melting rate compared to the fins and blades.

Figure 5 shows the evolution in time of the phase field ϕ parameter, which represents the liquid and melted phases in the computational domain, at Ra = 10,000.

At such a regime, the effect of convection is already appreciable, leading to the development of a curved melting front in the upper part of the computational domain, as expected from the literature [7,43,44]. Additionally in this case, the branched thermal support provides the best energy transfer to the PCM matrix compared to the fins and blades. At Ra = 50,000, the convection contribution is still increased, as shown in Figure 6.

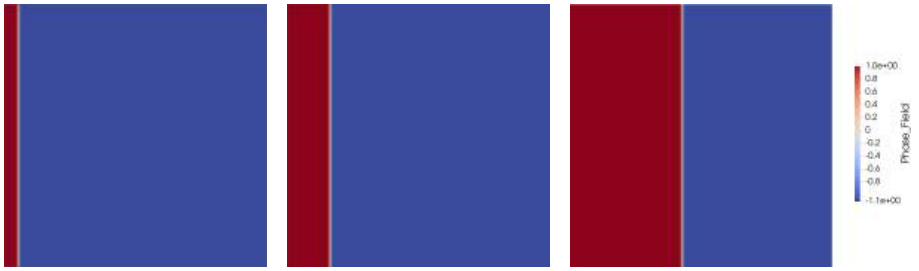

(**a**) $\theta = 10^{-3}$ (**b**) $\theta = 5 \times 10^{-3}$ (**c**) $\theta = 2.5 \times 10^{-2}$

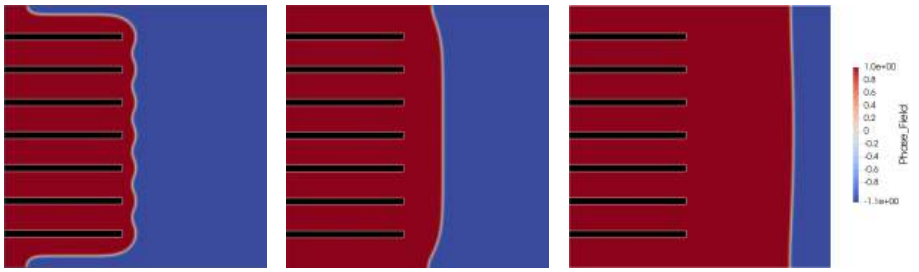

(**d**) $\theta = 10^{-3}$ (**e**) $\theta = 5 \times 10^{-3}$ (**f**) $\theta = 2.5 \times 10^{-2}$

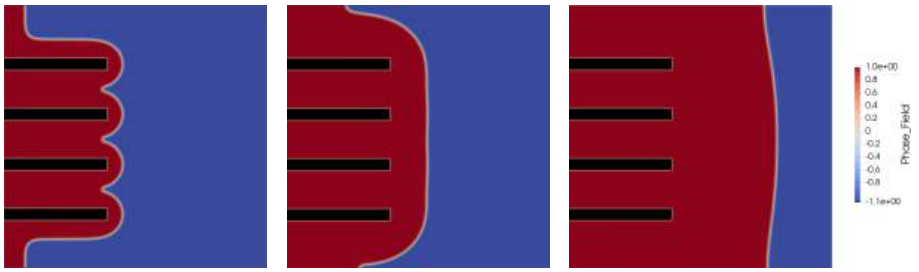

(**g**) $\theta = 10^{-3}$ (**h**) $\theta = 5 \times 10^{-3}$ (**i**) $\theta = 2.5 \times 10^{-2}$

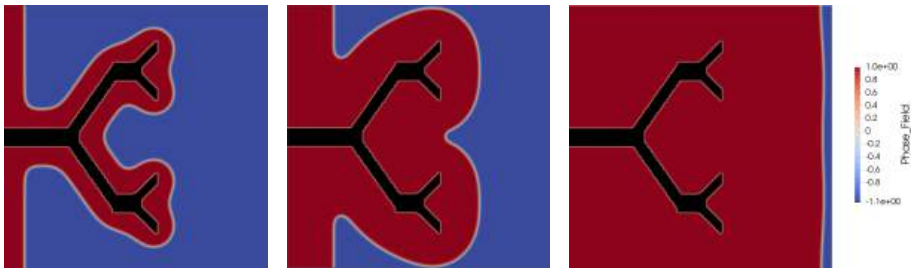

(**j**) $\theta = 10^{-3}$ (**k**) $\theta = 5 \times 10^{-3}$ (**l**) $\theta = 2.5 \times 10^{-2}$

Figure 4. Evolution in time of the phase field parameter ϕ as a function of the non-dimensional time θ. All panels refer to the cases at Ra $= 0$.

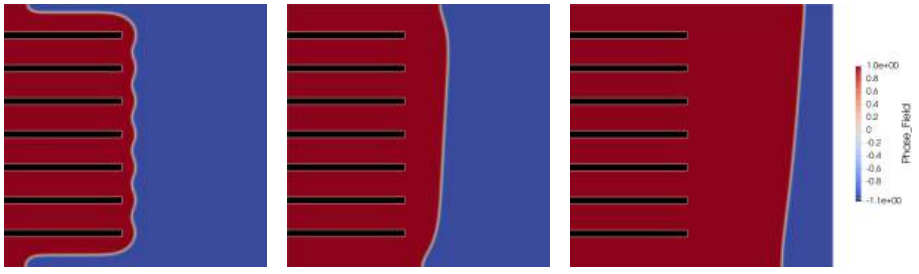

(**a**) $\theta = 10^{-3}$ (**b**) $\theta = 5 \times 10^{-3}$ (**c**) $\theta = 2.5 \times 10^{-2}$

Figure 5. *Cont.*

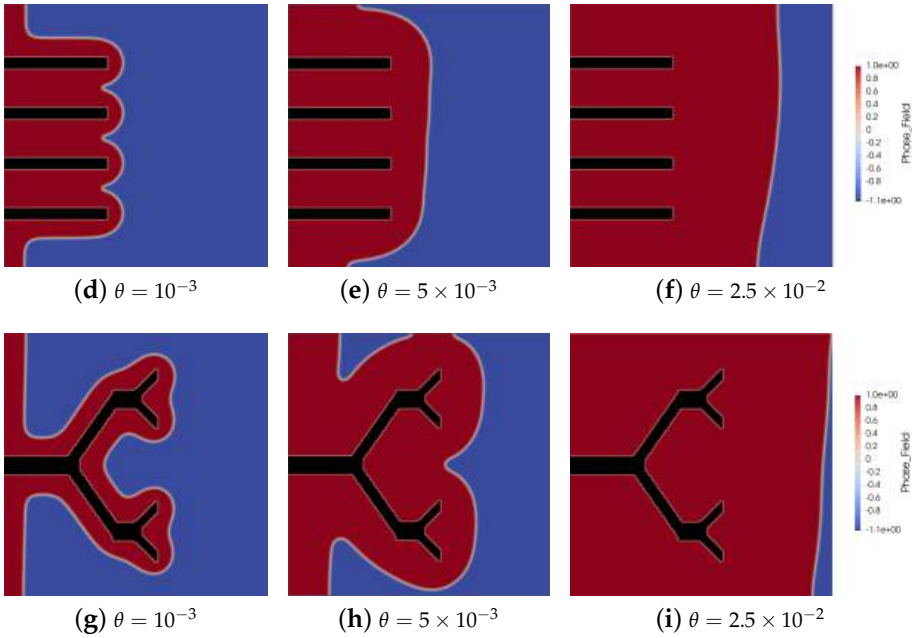

(**d**) $\theta = 10^{-3}$ (**e**) $\theta = 5 \times 10^{-3}$ (**f**) $\theta = 2.5 \times 10^{-2}$

(**g**) $\theta = 10^{-3}$ (**h**) $\theta = 5 \times 10^{-3}$ (**i**) $\theta = 2.5 \times 10^{-2}$

Figure 5. Evolution in time of the phase field parameter ϕ as a function of the non-dimensional time θ. All panels refer to the regime at Ra = 10,000.

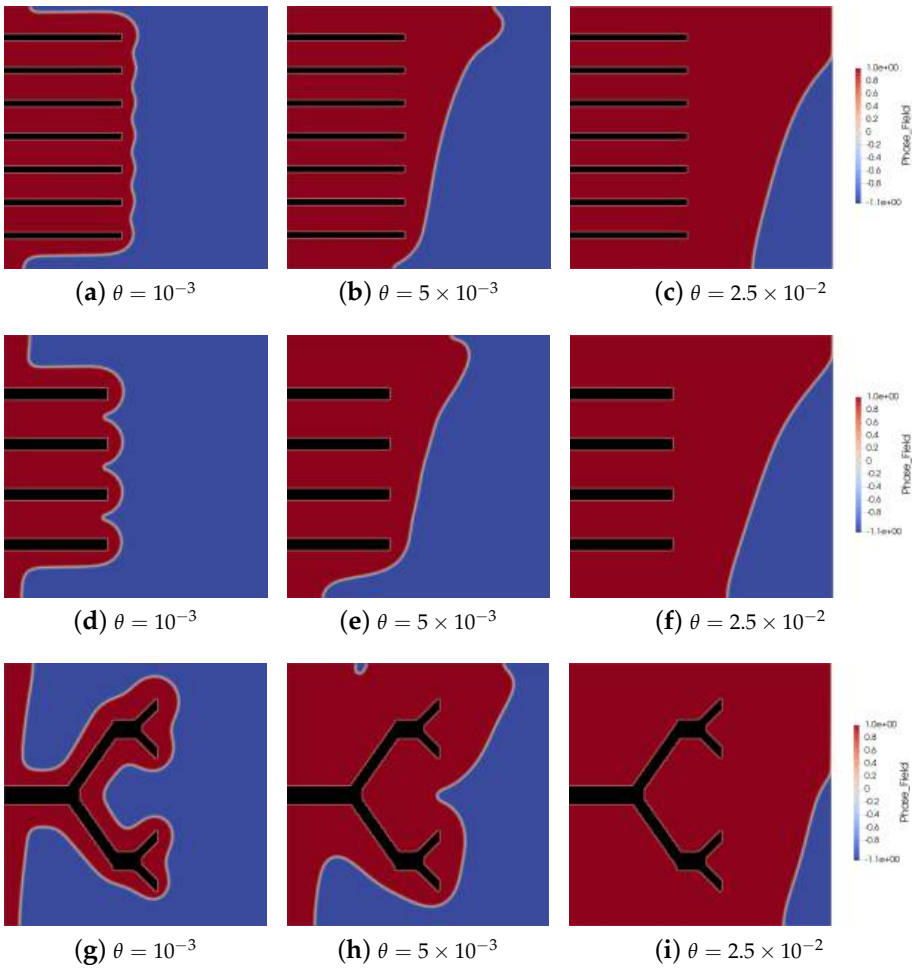

(**a**) $\theta = 10^{-3}$ (**b**) $\theta = 5 \times 10^{-3}$ (**c**) $\theta = 2.5 \times 10^{-2}$

(**d**) $\theta = 10^{-3}$ (**e**) $\theta = 5 \times 10^{-3}$ (**f**) $\theta = 2.5 \times 10^{-2}$

(**g**) $\theta = 10^{-3}$ (**h**) $\theta = 5 \times 10^{-3}$ (**i**) $\theta = 2.5 \times 10^{-2}$

Figure 6. Evolution in time of the phase field parameter ϕ as a function of the non-dimensional time θ. All panels refer to the regime at Ra = 50,000.

Figure 6 highlights the presence of secondary effects in the melting front due to the increased buoyancy. The variation in Ra, achieved through adjusting the module of g, causes the irregularities in the shape of the melting front, as expected from the literature for larger values of Ra [7,28,43,44]. Such effects are responsible for the anomalous performance reported in Figure 3d: to confirm this behavior, the phase field profiles at Ra = 500,000 for $\theta = 5 \times 10^{-3}$ are reported in Figure 7. It is also interesting to look at the velocity magnitude profiles inside the computational domain at such a large Ra value, as reported in Figure 8.

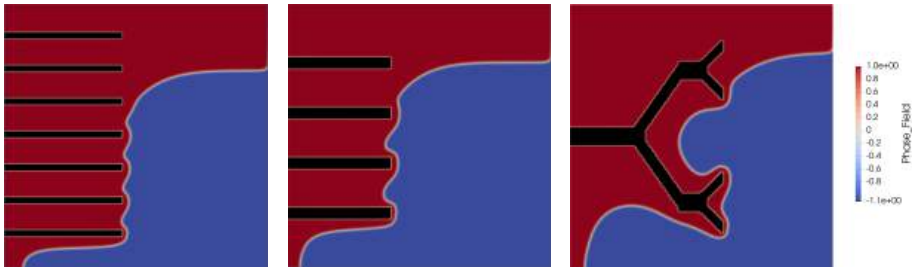

(**a**) (**b**) (**c**)

Figure 7. (**a**–**c**) Snapshots of the melting front position at Ra = 500,000 and $\theta = 5 \times 10^{-3}$.

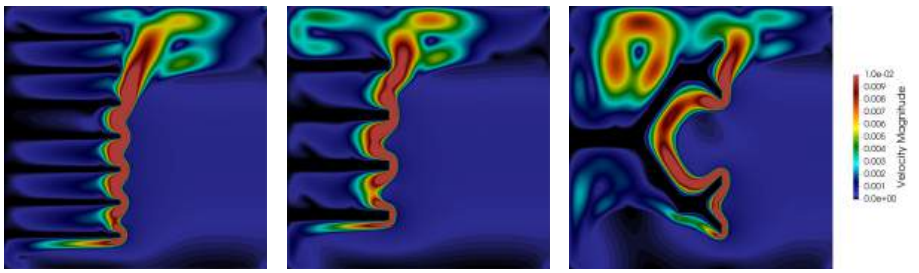

(**a**) (**b**) (**c**)

Figure 8. Contours of the velocity magnitude inside the computational domain for the three investigated geometries (**a**–**c**) at Ra = 500,000 and $\theta = 5 \times 10^{-3}$.

Figure 8 highlights the presence of convective patterns inside the melted portion of the domain, in line with the numerical and experimental findings in the literature [28,43,44]. Such convective patterns are known to play an important role in the evolution of the melted front [7], confirming the capability of fractal branched structures to promote their onset, thus enhancing the system power performance.

We wish to stress the versatility and stability of our algorithm, which capitalizes on the lightness and reliability of the LBM, coupled to the remarkable stability of the phase-field plugin, which allows fast and trustworthy predictions even without resorting to extreme resolutions or refinement algorithms.

4. Conclusions

In this paper, we have presented a three-phase approach for PCM-enhanced LHTES systems. Our methodology is based on a thermal 2D LBM implementation coupled to a phase-field plugin for the evaluation of melting front evolution in time. The model is light and versatile, yet the preliminary results provide reliable predictions on the evolution of non-trivial systems, in line with what expected from the literature. We have applied our model to investigate the thermal conductivity enhancement of the PCM matrix in the presence of thermal conductive supports in the form of fins, blades, and novel, branched fractal structures. Considering thermal supports of equal mass temperature and thermal conductivity, the novel, fractal layout consistently outperforms the more traditional ones in terms of PCM melting rates, delivering higher power performance.

Our three-phase thermal lattice Boltzmann model, coupled with phase-field analysis, demonstrates the superiority of fractal, branch-like structures as thermal conductive supports, which contributes to improving the melting rate of PCM-TES systems. These findings hold promise for advancing the efficiency of thermal energy storage technologies.

Author Contributions: Conceptualization, G.F.; Software, G.A.; Investigation, G.A., S.S. and G.F.; Writing—original draft, G.A., S.S. and G.F. All authors have read and agreed to the published version of the manuscript.

Funding: G.F. wishes to acknowledge the support of the Italian Government Grants PRIN 2022F422R2 and PRIN P202298P25; S.S. acknowledges financial support from the European Research Council under the Horizon 2020 Programme Advanced Grant agreement no. 739964 ('COPMAT').

Data Availability Statement: All data and codes are available upon request to the corresponding author.

Acknowledgments: The authors wish to acknowledge and kindly thank Patrik Hoffmann, Head of the laboratory for Advanced Materials Processing, EMPA, Switzerland, for proposing the fractal approach for improving the total efficiency of the PCM in combination with hydrogen storage, and for fruitful discussions during the entire work.

Conflicts of Interest: The authors declare no conflict of interest.

References

1. Mahon, H.; O'Connor, D.; Friedrich, D.; Hughes, B. A review of thermal energy storage technologies for seasonal loops. *Energy* **2022**, *239*, 122207. [CrossRef]
2. IEA. Renewables. 2019. Available online: https://www.iea.org/reports/renewables-2019 (accessed on 22 February 2023).
3. Gutierrez, A.; Miró, L.; Gil, A.; Rodríguez-Aseguinolaza, J.; Barreneche, C.; Calvet, N.; Py, X.; Fernández, A.I.; Grágeda, M.; Ushak, S.; et al. Advances in the valorization of waste and by-product materials as thermal energy storage (TES) materials. *Renew. Sustain. Energy Rev.* **2016**, *59*, 763–783. [CrossRef]
4. Sadeghi, G. Energy storage on demand: Thermal energy storage development, materials, design, and integration challenges. *Energy Storage Mater.* **2022**, *46*, 192–222. [CrossRef]
5. Gunasekara, S.N.; Barreneche, C.; Inés Fernández, A.; Calderón, A.; Ravotti, R.; Ristić, A.; Weinberger, P.; Ömur Paksoy, H.; Koçak, B.; Rathgeber, C.; et al. Thermal energy storage materials (TESMs)–What does it take to make them fly? *Crystals* **2021**, *11*, 1276. [CrossRef]
6. Guo, S.; Liu, Q.; Zhao, J.; Jin, G.; Wu, W.; Yan, J.; Li, H.; Jin, H. Mobilized thermal energy storage: Materials, containers and economic evaluation. *Energy Convers. Manag.* **2018**, *177*, 315–329. [CrossRef]
7. Facci, A.L.; Lauricella, M.; Succi, S.; Villani, V.; Falcucci, G. Optimized modeling and design of a PCM-enhanced H2 storage. *Energies* **2021**, *14*, 1554. [CrossRef]
8. Cabeza, L.F.; Castell, A.; Barreneche, C.d.; De Gracia, A.; Fernández, A. Materials used as PCM in thermal energy storage in buildings: A review. *Renew. Sustain. Energy Rev.* **2011**, *15*, 1675–1695. [CrossRef]
9. Cabeza, L.F. Advances in thermal energy storage systems: Methods and applications. In *Advances in Thermal Energy Storage Systems*; Elsevier: Amsterdam, The Netherlands, 2021; pp. 37–54.
10. Nazir, H.; Batool, M.; Osorio, F.J.B.; Isaza-Ruiz, M.; Xu, X.; Vignarooban, K.; Phelan, P.; Kannan, A.M. Recent developments in phase change materials for energy storage applications: A review. *Int. J. Heat Mass Transf.* **2019**, *129*, 491–523. [CrossRef]
11. Mahdi, J.M.; Lohrasbi, S.; Nsofor, E.C. Hybrid heat transfer enhancement for latent-heat thermal energy storage systems: A review. *Int. J. Heat Mass Transf.* **2019**, *137*, 630–649. [CrossRef]
12. Sedeh, M.M.; Khodadadi, J. Thermal conductivity improvement of phase change materials/graphite foam composites. *Carbon* **2013**, *60*, 117–128. [CrossRef]
13. Wei, G.; Wang, G.; Xu, C.; Ju, X.; Xing, L.; Du, X.; Yang, Y. Selection principles and thermophysical properties of high temperature phase change materials for thermal energy storage: A review. *Renew. Sustain. Energy Rev.* **2018**, *81*, 1771–1786. [CrossRef]
14. Almonti, D.; Mingione, E.; Tagliaferri, V.; Ucciardello, N. Design and analysis of compound structures integrated with bio-based phase change materials and lattices obtained through additive manufacturing. *Int. J. Adv. Manuf. Technol.* **2021**, *119*, 149–161. [CrossRef]
15. Warzoha, R.J.; Fleischer, A.S. Effect of graphene layer thickness and mechanical compliance on interfacial heat flow and thermal conduction in solid–liquid phase change materials. *ACS Appl. Mater. Interfaces* **2014**, *6*, 12868–12876. [CrossRef] [PubMed]
16. Li, M.; Mu, B. Effect of different dimensional carbon materials on the properties and application of phase change materials: A review. *Appl. Energy* **2019**, *242*, 695–715. [CrossRef]
17. Sarbu, I.; Dorca, A. Review on heat transfer analysis in thermal energy storage using latent heat storage systems and phase change materials. *Int. J. Energy Res.* **2019**, *43*, 29–64. [CrossRef]
18. Succi, S. *The lattice Boltzmann Equation for Fluid Dynamics and Beyond*; Clarendon: Oxford, UK, 2001.

19. Krüger, T.; Kusumaatmaja, H.; Kuzmin, A.; Shardt, O.; Silva, G.; Viggen, E.M. *The Lattice Boltzmann Method*; Springer: Berlin/Heidelberg, Germany, 2017; Volume 10, pp. 978–983.
20. Miller, W.; Succi, S.; Mansutti, D. Lattice Boltzmann model for anisotropic liquid-solid phase transition. *Phys. Rev. Lett.* **2001**, *86*, 3578. [CrossRef]
21. Falcucci, G.; Amati, G.; Fanelli, P.; Krastev, V.K.; Polverino, G.; Porfiri, M.; Succi, S. Extreme flow simulations reveal skeletal adaptations of deep-sea sponges. *Nature* **2021**, *595*, 537–541. [CrossRef]
22. Falcucci, G.; Polverino, G.; Porfiri, M.; Amati, G.; Fanelli, P.; Krastev, V.K.; Succi, S. Reply to: Models of flow through sponges must consider the sponge tissue. *Nature* **2022**, *603*, E26–E28. [CrossRef]
23. Krastev, V.; Falcucci, G. Simulating engineering flows through complex porous media via the lattice Boltzmann method. *Energies* **2018**, *11*, 715. [CrossRef]
24. Falcucci, G.; Chiatti, G.; Succi, S.; Mohamad, A.A.; Kuzmin, A. Rupture of a ferrofluid droplet in external magnetic fields using a single-component lattice Boltzmann model for nonideal fluids. *Phys. Rev. E Stat. Nonlinear Soft Matter Phys.* **2009**, *79*, 056706. [CrossRef]
25. Sbragaglia, M.; Benzi, R.; Biferale, L.; Succi, S.; Sugiyama, K.; Toschi, F. Generalized lattice Boltzmann method with multirange pseudopotential. *Phys. Rev. E* **2007**, *75*, 026702. [CrossRef] [PubMed]
26. Falcucci, G.; Bella, G.; Chiatti, G.; Chibbaro, S.; Sbragaglia, M.; Succi, S. Lattice Boltzmann Models with Mid-Range Interactions. *Comm. Comput. Phys.* **2007**, *2*, 1071–1084.
27. Colosqui, C.E.; Falcucci, G.; Ubertini, S.; Succi, S. Mesoscopic simulation of non-ideal fluids with self-tuning of the equation of state. *Soft Matter* **2012**, *8*, 3798–3809. [CrossRef]
28. Huber, C.; Parmigiani, A.; Chopard, B.; Manga, M.; Bachmann, O. Lattice Boltzmann model for melting with natural convection. *Int. J. Heat Fluid Flow* **2008**, *29*, 1469–1480. [CrossRef]
29. Pareschi, G.; Frapolli, N.; Chikatamarla, S.S.; Karlin, I.V. Conjugate heat transfer with the entropic lattice Boltzmann method. *Phys. Rev. E* **2016**, *94*, 013305. [CrossRef]
30. Chiappini, D.; Donno, A. A comparison between different fractal grid generation methods coupled with lattice Boltzmann approach. *AIP Conf. Proc.* **2016**, *1738*, 270003.
31. Chiappini, D. A coupled lattice Boltzmann-finite volume method for phase change material analysis. *Int. J. Therm. Sci.* **2021**, *164*, 106893. [CrossRef]
32. Wu, S.; Yan, T.; Kuai, Z.; Pan, W. Thermal conductivity enhancement on phase change materials for thermal energy storage: A review. *Energy Storage Mater.* **2020**, *25*, 251–295. [CrossRef]
33. Joshi, V.; Rathod, M.K. Experimental and numerical assessments of thermal transport in fins and metal foam infused latent heat thermal energy storage systems: A comparative evaluation. *Appl. Therm. Eng.* **2020**, *178*, 115518. [CrossRef]
34. Li, J.; Zheng, Y.; Liu, X. Enhancing discharging performance of a phase change thermal storage unit with a fractal space-filling matrix. *J. Renew. Sustain. Energy* **2021**, *13*, 014102. [CrossRef]
35. Yu, C.; Wu, S.; Huang, Y.; Yao, F.; Liu, X. Charging performance optimization of a latent heat storage unit with fractal tree-like fins. *J. Energy Storage* **2020**, *30*, 101498. [CrossRef]
36. Succi, S. *The Lattice Boltzmann Equation: For Complex States of Flowing Matter*; Oxford University Press: Oxford, UK, 2018.
37. Ben Ltaifa, K.; D'Orazio, A.; Dhahri, H. Numerical analysis of mixed convection heat transfer and laminar flow in a rectangular inclined micro-channel totally filled with Water/Al_2O_3 Nano fluid. *J. Therm. Anal. Calorim.* **2021**, *144*, 2465–2482. [CrossRef]
38. Miller, W.; Succi, S. A lattice Boltzmann model for anisotropic crystal growth from melt. *J. Stat. Phys.* **2002**, *107*, 173–186. [CrossRef]
39. D'Orazio, A.; Karimipour, A.; Mosavi, A. Develop lattice Boltzmann method and its related boundary conditions models for the benchmark oscillating walls by modifying hydrodynamic and thermal distribution functions. *Eur. Phys. J. Plus* **2020**, *135*, 915. [CrossRef]
40. Chandrasekhar, S. *Hydrodynamic and Hydromagnetic Stability*; Courier Corporation: Chelmsford, MA, USA, 2013.
41. Chaabane, R.; Kolsi, L.; Jemni, A.; Alshammari, N.K.; D'Orazio, A. Numerical study of the Rayleigh–Bénard convection in two-dimensional cavities heated by elliptical heat sources using the lattice Boltzmann method. *Phys. Fluids* **2021**, *33*, 123605. [CrossRef]
42. Pelusi, F.; Lulli, M.; Sbragaglia, M.; Bernaschi, M. TLBfind: A Thermal Lattice Boltzmann code for concentrated emulsions with FINite-size Droplets. *Comput. Phys. Commun.* **2022**, *273*, 108259. [CrossRef]
43. Jany, P.; Bejan, A. Scaling theory of melting with natural convection in an enclosure. *Int. J. Heat Mass Transf.* **1988**, *31*, 1221–1235. [CrossRef]
44. Bertrand, O.; Binet, B.; Combeau, H.; Couturier, S.; Delannoy, Y.; Gobin, D.; Lacroix, M.; Le Quéré, P.; Médale, M.; Mencinger, J.; et al. Melting driven by natural convection A comparison exercise: First results. *Int. J. Therm. Sci.* **1999**, *38*, 5–26. [CrossRef]